ENHANCED ELECTRICAL PROPERTIES OF NONSTRUCTURAL CUBIC SILICON CARBIDE WITH GRAPHENE CONTACT FOR PHOTOVOLTAIC APPLICATIONS

M. N. RASHEED[a,*], A. MARYAM[a], K. FATIMA[a], F. IQBAL[a], M. AFZAL[b,c], M. SYVÄJÄRVI[d], H. MURTAZA[e,] B. ZHU[f], M. ASGHAR[g]

[a]*Department of Physics, The Islamia University of Bahawalpur, Bahawalpur-63100, Pakistan*

[b]*Department of Energy Techology, KTH Royal Institute of Technology, Stockholm-10465, Sweden*

[c]*Hubei Collaborative Innovation Center for Advanced Organic Chemical Materials, Faculty of Physics and Electronic Science, Hubei University Wuhan, Hubei 430062, P.R China*

[d]*Department of Physics, Chemistry and Biology, Linköping University, IFM, SE-58183 Linköping, Sweden*

[e]*Department of Biochemistry and Biotechnology, The Islamia University of Bahawalpur, Bahawalpur-63100, Pakistan*

[f]*School of energy and environment, Southeast University, Nanjing, China*

[g]*Department of Physics , Khawaja Fareed University of Engineering and Information Technology, Rahim Yar Khan-64200, Pakistan*

Cubic silicon carbide (3C-SiC) is successfully synthesized through a simple solid-state reaction technique at a comparatively low temperature without using any catalyst. The XRD data is also used to study other structural parameters of synthesized sample by using different method. Raman peak at 796 cm^{-1} supports the XRD results. Si–C vibrational mode observed at 788 cm^{-1} in the FTIR spectrum further confirms the growth of 3C-SiC. UV-Vis spectroscopy is used to measure optical bandgap energy (E_g = 2.36 eV). Other optical parameters such as dielectric constant and refractive index of grown sample are also studied. Electrical performance is analyzed by using graphene contact with further evaluation of dark and light IV-measurements. The use of graphene contact establishes the enhancement of electrical conductivity of as-grown samples particularly when they are exposed to light. These findings indicate that the grown sample has comparatively better transport properties than conventional metal contacts under the illuminated conditions.

(Received June 18, 2020; Accepted September 30, 2020)

Keywords: 3C-SiC, Solid-state reaction, Graphene, I-V, XRD, Optical conductivity

1. Introduction

Silicon carbide (SiC) is among the most investigated compound of fullerene and silicon having a wide bandgap with particular electric, thermal, chemical and mechanical properties which make it a suitable candidate for high-temperature, high frequency and high energy power applications. There are recently reported various technological applications of this material other than its conventional usage for instance as a support material for growth of graphene [1], light-emitting diodes [2], photocatalysis [3], Li-Ion battery [4], high-temperature gas sensors [5], and for hydrogen production and storage [6]. Study of as-grown SiC by using fullerene as a carbon precursor along with a graphene contact is a serious challenge for many electronic devices that provide insight towards the synthesis of suitable material for high-temperature applications [7]. Recently, Katsuhiko Ariga et al published a review article on various functional possibilities of fullerene in light energy conversion applications [8]. SiC is IV-IV semiconductor compound having more than 230 stable polytypes [9]. The energy band gap of most common SiC polytypes i.e. 3C, 4H and 6H is 2.4 eV, 3.2 eV and 3.34 eV, respectively [10, 11].

* Corresponding authors: naveed@iub.edu.pk

Presently very sophisticated techniques are used to synthesize SiC and their polytypes such as arc-discharge method [12], laser ablation method [13], chemical vapor reaction (CVR) [14], chemical vapor deposition (CVD) [15,16], sol-gel [17,18], hot press [19], and ball milling [20]. Most of these techniques require high temperature > 1500^{o}C with complex and sophisticated procedures that are too much energy and time consuming [21]. There is recent trend to explore simpler routes to synthesize this material so that it may help to add ease in construction of above mentioned electronic devices that also leads the path towards its commercial viability [22]. The structures, size, and morphology of grown SiC polytypes depend on synthesizing techniques. The carbothermal reduction and sol-gel methods were applied to fabricate SiC nanorods, nanowires from tetraethyl orthosilicate (TEOS) and phenolic resins [23, 24]. In order to decrease the sintering temperature and growth time, high pressure is applied [25]. However, many reports on the synthesis methods of SiC nanoparticles also showed some shortcomings, like excessive use of instrumentation, operational complexes, low purity, slow growth rate, high temperature and need of a catalyst [26].

Electrical properties of 3C-SiC were studied which showed very low conductivity due to synthesis defects or the impurities present by using different catalysts [27]. The transparent 2D graphene is an excellent conductor due to its electrical, and optical properties[28-30]. In principle, the electrons in the monolayer graphene sheets swap over the entire sheet to provide the charge to transport through an atomic level thick material with very little optical absorption [27]. M. Portail et al. studies the electrical properties of graphene grown by CVD on 3C–SiC/Si at different pressure but there is a need to control over deposition on various faces of 3C-SiC that play a crucial role in conducting behaviors of grown samples [31].

In the present work, the solid-state reaction method is used for the synthesis of 3C-SiC by mixing fullerene (C-60) and silicon at a high pressure of 110 MPa and without adding any catalyst. The present method has a high growth rate and also required comparatively low temperature for dangling bond activation at high pressure. Structural, optical, and electrical parameters are studied by using XRD, UV-vis, Raman FTIR, and, I-V measurements. Graphene contact on the SiC surface substantially improved the electrical properties of the grown sample. IV measurements of grown samples are extensively studied for future application of this material for photovoltaics by a comparison of obtained results with dark and light illumination. The purpose of I-V measurements under light is to study the parameters that lead to figure out the challenges of a sustainable and functional photovoltaic material.

2. Experimental work

2.1. Synthesis

3C-SiC is synthesized by using a modified programmable muffle furnace. Pure silicon (99.99 %) powder and fullerene were purchased from Sigma Aldrich. The synthesis procedure is started by mixing silicon and fullerene pure powders in weight ratio 1:1 with motor and pestle. The mixed powders were loaded uniaxially under the pressure of 110 MPa and converted into a pellet. This high pressure activates the dangling bonds of silicon and fullerene to establish SiC structure at low temperature [32]. After the formation of the pellet, it was placed in an alumina crucible and loaded in the hot zone of the furnace with a heating capacity range of temperature 1800^{o}C. Samples were sintered at 1280^{o}C, 1380^{o}C and 1480^{o}C @10^{o}C/min and argon gas with a purity of 99% flowed at a constant flow rate 200 sccm in the furnace and kept for 3 hours where 3C-SiC is finally grown. The furnace was naturally cooled to room temperature and argon flow was stopped; greenish color was material is obtained.

2.2. Characterization techniques

As grown samples were characterized by the diverse state of the art techniques as envisaged in Table 1.

Table 1. Detail of the Characterization Techniques

Sr.#	Name of characterization measurement	Name of equipment	Equipment detail	Measurement detail
1	X-ray diffraction	Bruker D8 Advance	Cu Kα radiation (40 kV, 35 mA, λ = 1.5406 Å) in the angular range of 20°–80° with the scan speed of 0.02°/sec.	Crystal structure of the sample
2	RAMAN	Horiba Jabin spectrometer	20 mW He-Ne LASER, range 300-1000 cm^{-1}	To find out allowed characteristic optical modes of the lattice
3	UV-vis	Cary 60 UV-Vis – Agilent	Double Beam Wavelength: 190 – 800nm Resolution: 1.5 nm Light source: Xenon Flash Lamp (80 Hz)	To study the optical properties
4	FT-IR	Bruker Tensor 27A	Attentive total reflection (ATR) mode	To explore the lattice vibration of the sample
5	Voltage current	4 probe vacuum station	Inlet gases O_2 and N_2 maximum temperature is 250°C, minimum pressure is 10^{-6} Torr	To quantify the transport properties of charge carriers

3. Results and discussion

3.1. Structural properties

X-ray diffraction (XRD) pattern of as-grown silicon carbide annealed at different temperatures 1280°C, 1380°C and 1480°C for 3 hours and represented as (a), (b) and (c) respectively is shown in Fig. 1. XRD pattern of sample (a) showed that there is no proper phase transformation and unreacted fullerene and silicon are still present there. A very small peak at 36°C indicates the formation of silicon carbide. Sample (b) also has a similar pattern similar to sample (a) showing no phase transformation. Whereas sample (c) displays the complete phase transformation to 3C-SiC but residuals of Si and C are still present. This indicates the optimum temperature required for SiC synthesis without any catalyst is 1480°C and hereafter all calculations are performed on sample (c). The diffraction peaks appeared at 2θ values at 35.90°, 41.64°, 60.29° and 72.08° corresponding to Miller planes (1 1 1), (2 0 0), (2 2 0) and (3 1 1) respectively, have confirmed the formation of the cubic structure of synthesized SiC which are well consistent with the literature [33]. The peak at 2θ = 22°, 28° and 31° are assigned to carbon (fullerene), silicon and silicon dioxide respectively. The interplanar spacing (d_{hkl}) of 3C-SiC powder is calculated using Bragg's Eq. (1) are tabulated in Table 2.

$$2d_{hkl}\sin\theta = n\lambda \quad (1)$$

The volume of the unit cell of 3C-SiC is calculated by using simple relation: a^3. Lattice parameter (a) are calculated using the Eq. (2), Crystallite size (D) by Scherrer Eq. (3), Strain (ε), dislocation density (δ), and X-rays density related to each plane are calculated by Eq.'s (4), (5), and (6) respectively and represented in Table 2 [34].

$$d^2 = (h^2 + k^2 + l^2)/a^2 \quad (2)$$

$$D = k\lambda/\beta\cos\theta \quad (3)$$

where; k is a constant and its value is 0.9, λ is wavelength of incident x-rays, β is full width at half maximum (FWHM), θ is the Bragg's angle.

$$\varepsilon = \beta_{hkl}/4\tan\theta \quad (4)$$

$$\delta = 1/D^2 \quad (5)$$

$$(\Delta x) = \frac{8M}{Na^3} \quad (6)$$

The average crystallite size, dislocation density and strain of the typical sample (c) were also calculated by the Scherrer method, Scherrer plot method, Williamson–Hall (W-H) method and Size strain plot (SSP) method and represent in Table 3. [35,36] . The detail of each is described below:

3.1.1. Scherrer plot method

The crystalline size and strain affect the peak broadening and effects crystal imperfection. The peak broadening depends upon both samples and instruments broadening.

The instrumental broadening β_{hkl} was modified, related to each diffraction peak of the sample (c) by using Eq. (7) [35].

$$\beta_{hkl} = \sqrt{(\beta_{hkl})^2_{Measured} - (\beta_{hkl})^2_{Instrumental}} \quad (7)$$

By using Eq.'s (3) and (7), the following relation is obtained

$$D = k\lambda / \beta_{hkl}\cos\theta \quad \Rightarrow \cos\theta = k\lambda / D\beta_{hkl} \quad (8)$$

A plot of cosθ vs $1/\beta_{hkl}$ associated with the sample (c) using the Eq. (8) shown in Fig. 2(a) and the slope of linear fit gives the crystalline size. The results obtained from the Scherrer plot method are listed in Table 3.

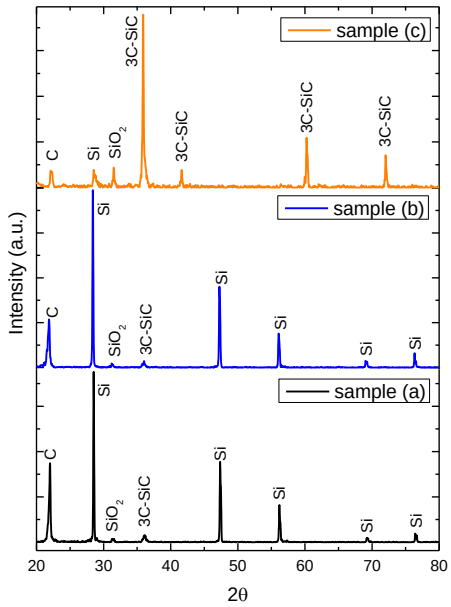

Fig. 1. (a) XRD spectra of samples annealed at 1280°C, 1380°C and 1480°C .

3.1.2. Williamson–Hall plot method

The uniform deformation model (UDM) is used to estimate crystalline size, dislocation density, and strain [36]. The strain-induced in the sample (c) was calculated using Eq. (7). From Eq.

(3) and (4), it is observed that the W-H method is not fallow1/cos θ but depends on tan θ. If the particle size and strain contributions to the line width are self-governing, and both have a Cauchy-like profile and the observed line width is just the sum of Eq.'s (3) and (4) so that Eq. (9) is obtained. To calculate the average particle size, strain, and dislocation density, a plot between $\beta_{hkl}\ cos\ \theta$ vs $4sin\ \theta$ for all XRD peaks of sample (c) is drawn as shown in Fig. 2(b). Linear fitting the given data; strain and crystallite size are calculated from the y-intercept and slope, respectively and are tabulated in Table 3.

$$\beta_{hk} = k\lambda / \beta_{hkl} \cos\theta + 4\varepsilon \tan\theta \quad (9)$$

Rearranging it we get

$$\beta_{hkl}\cos\theta = k\lambda / D + 4\varepsilon \tan\theta \quad (10)$$

Eq. (10) describes the uniform deformation Model (UDM), here strain (ε) is considered as same in all crystallographic directions in the material. The results for sample (c) calculated from UDM analysis are demonstrated in Fig. 2(b) and the results are presented in Table 3.

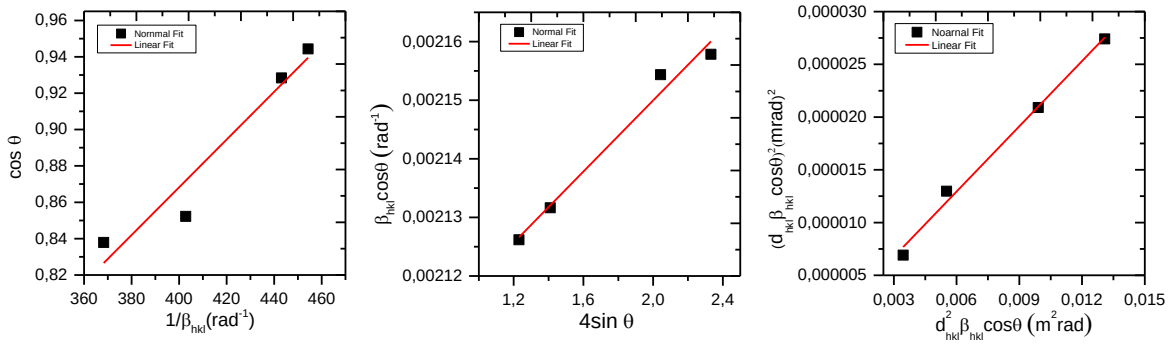

Fig. 2. XRD analysis of, (a) Scherrer plot, (b) Williamson plot, (c) Size-strain plot.

3.1.3. Size-strain method

Williamson–Hall method yields micro strain contribution associated with the line broadening in the XRD spectrum. On the other hand, the size strain method is very useful to calculate the size and strain due to the isotropic-assisted line broadening [Fig. 2(c)]. Consequently, the profile of crystallite size and strain represented by Lorentzian and Gaussian functions are calculated with the help of Eq. (11)[35].

$$(d_{hkl}\beta_{hkl}cos\theta)^2 = k/D\left(d_{hkl}^2\beta_{hkl}cos\theta\right) + (\varepsilon/2)^2 \quad (11)$$

where d_{hkl} is lattice constant and k is fitting constant and it depends upon the shape of the particle.

Fig. 2(c) displays the relationship between $(d_{hkl}\beta_{hkl}Cos\theta)^2$ and $\left(d_{hkl}^2\beta_{hkl}cos\theta\right)$. The slope of the fitted line gives the value of the crystalline size and the strain was calculated by y-intercept. The evaluated microstructural parameters of sample (c) are summarized in Table 3.The results obtained by all these methods support each other.

Table 2. Calculated values of Lattice parameter (a), Interplanar spacing (d_{hkl}), volume (V), X-rays density, crystallite size (D), strain (ε), and Dislocation density (δ) of β-SiC.

Angle 2θ	Miller indices (h k l)	Lattice parameter (a) (Å)	Interplanar spacing (d_{hkl}) (Å)	Volume (V) $(Å)^3$	X-rays density (Δx)	Crystallite size (D) (nm)	Strain (ε) 10^{-10}	Dislocation density (δ) 10^{-10}
35.90	1 1 1	4.33	2.499	81.36	6.545	39.60	9.1	6.4
41.64	2 0 0	4.34	2.167	81.88	6.522	39.31	9.2	6.5
60.29	2 2 0	4.34	1.535	81.85	6.505	35.32	10	8
72.06	3 1 1	4.35	1.311	82.17	6.482	41.31	8.8	5.9

Table 3. Structure parameters of as grown sample (c).

Dislocation Density(δ) $(10^{-3}$ nm$^{-2})$			Average crystallite (nm)				Strain (με)			
Scherrer Eq.	W-H	SSP	Scherrer	Scherrer Plot	W-H	SSP	Scherrer Eq.	Scherrer Plot	W-H	SSP
0.22	0.21	0.20	40.56	114.93	69.29	70.30	0.366	0.366	0.280	0.057

3.2. Optical measurements

Metallic, nonmetallic and semiconductor materials are simply classified based upon optical absorption parameter. The optical band gap and other optical parameters that are mentioned below are calculated using UV-vis spectroscopic.

3.2.1. Optical band gap

The optical bandgap of sample (c) is calculated from the absorbance spectrum. The relationship between the absorption coefficient and photon energy is given by the Davis and Mott equation. By using the Tauc plot [37], the bandgap of the 3C-SiC is determined. Tauc plot is drawn between the $(\alpha h\upsilon)^{1/2}$ and incident photon energy (hυ) given by Eq.(12) and shown in Fig. 3 that gives the value of bandgap which is 2.36 eV for sample (c) and well consistent with the optical band gap of 3C-SiC [38].

$$\alpha h\upsilon = C\,(h\upsilon - E_g)^n \tag{12}$$

where, C is a constant, E_g is optical bandgap energy of the material, and n depends on the type of direct or indirect bandgap of the material here n = ½ as SiC has indirect bandgap

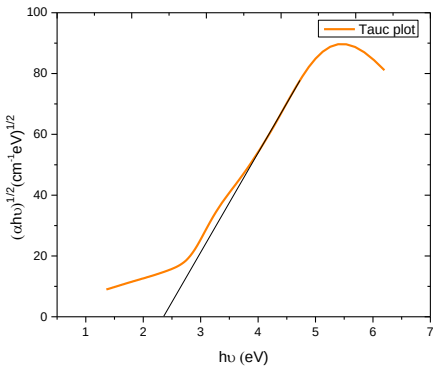

Fig. 3. Energy band gap plot (Tauc plot) of 3C-SiC.

3.2.2. Dielectric constants

One of the fundamental intrinsic properties of optical material is a dielectric constant whose real part represents the retardation of light in the material whereas the imaginary part represents the absorbance of energy from the electric field due to dipole motion.

The real (ε_r) and imaginary part (ε_i) of dielectric constant are calculated by Eq.'s (13) and (14).

$$\varepsilon_r = n^2 - k^2 \tag{13}$$

$$\varepsilon_i = 2nk \tag{14}$$

Here, *k* and *n* are the extinction coefficient and refractive index respectively.

Fig. 4(a) represents real and imaginary parts of dielectric constant as a function of the wavelength which illustrates that the real part nearly remains constant for $\lambda > 450$ nm and then exponentially decreases for 240 nm $< \lambda <$ 450 nm and increases for lower wavelength whereas the imaginary part remains almost constant for $\lambda > 450$ nm and then increases with decrease in wavelength exponentially and it decreases for lower wavelength. The free carrier contribution to absorption is confirmed by the imaginary part of dielectric constants [39].

3.2.3. Refractive index

For the fabrication of optical devices based on phase velocity, polarization and local field of the material, the refractive index plays an important role. It is given by the Eq. (15)

$$n(\lambda) = n_o + \frac{A}{\lambda^2} + \frac{B}{\lambda^2} \tag{15}$$

where n_0, A and B are the Cauchy's parameters and its graph between refractive index and wavelength for sample (c) is shown in Fig. 4(b) This shows that for large wavelengths, the refractive index is constant and it decreases exponentially for 235 nm $< \lambda <$ 450 nm. The refractive index of sample (c) is 0.275. Normal dispersion behavior appears for the exponential decrease in the refractive index [37].

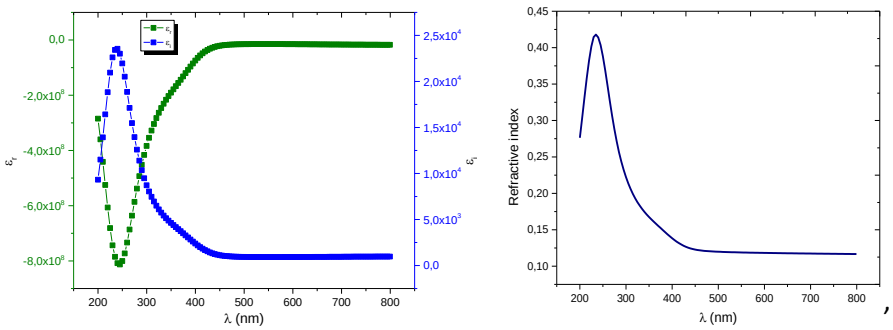

a) *b)*

Fig. 4. Optical parameter of cubic silicon carbide (a) dielectric constant (real ε_r and imaginary part), (b) refractive index.

3.3. RAMAN spectroscopy analysis

The vibrational and structural properties of grown samples are studied by Raman spectroscopy. Raman spectra for samples (a), (b), and (c) are recorded and shown in Fig. 5. It is clear from the figure that sample (c) has the Raman peak at 796 cm^{-1} and 521cm^{-1} corresponds to SiC and amorphous silicon respectively [40]. The peak at 796 cm^{-1} can correlate to longitudinal optical (LO) phonons mode of 3C-SiC that only appears in sample (c) The Raman results also support the XRD and FTIR results.

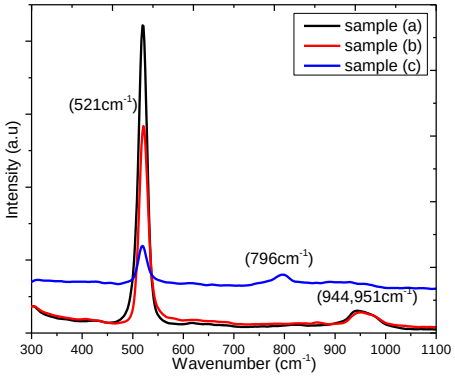

Fig. 5. Raman graph of cubic silicon carbide.

3.4. FTIR analysis

FTIR is used to study the vibrational frequency and chemical composition of grown materials. FTIR peaks at lower wavenumber i.e. 500 nm - 700 nm are assigned to metal oxides which may be appeared due to the formation of SiO_2. The transversal optic (TO) mode of Si-C approximately appeared at ~788 cm^{-1} and C-C vibrations at one shoulder corresponding to the longitudinal optic (LO) mode of the Si-C vibrations is identified at 860–950 cm^{-1} as shown in Fig. 6. The result is consistent with previous reports [41]. The 788 cm^{-1} peaks, corresponding to the Si-C vibration is intensified and widened significantly

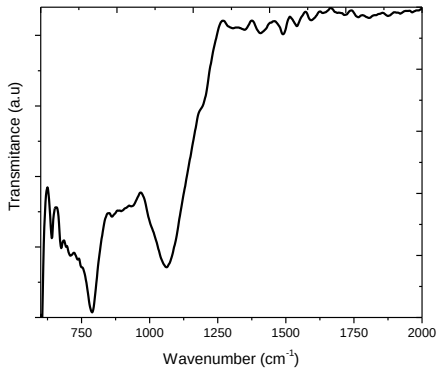

Fig. 6. FTIR spectrum of the cubic silicon carbide.

3.5. I-V measurements

I-V measurements of our grown sample (c) are studied with graphene contact and we further explore the conductivity enhancement of this sample with exposure of visible light. 3C-SiC with the graphitic phase is already reported with enhanced I-V characteristics of CVD grown samples of 3C-SiC. I-V measurement was performed with silver and graphene contact in the vacuum probe station in ambient conditions. For this purpose, a graphene monolayer was transferred on the half surface of the sample on which a silver contact was made. Further IV measurements were performed under the illumination of light having wavelength 375nm and power 23mW. The conductivity of 3C-SiC with graphene contact increases due to the high conducting response of graphene, the conductivity reaches 0.763 mA for applied voltage 5 volt as shown in Fig. 7. This enhances the electrical conductivity to 3.57 mA when exposing to light. It is recommended that the graphene contact is a better option for the photovoltaic applications of 3C-SiC as the I-V curve with and without graphene clearly shows the transition of material behavior from insulating to semiconducting and then further enhancement of conductivity through exposure to light. These findings suggest that the graphene monolayer doesn't

limit the current flow but it enhances the conductivity of our grown sample (c) that's a requirement for application of 3C-SiC in energy technological applications.

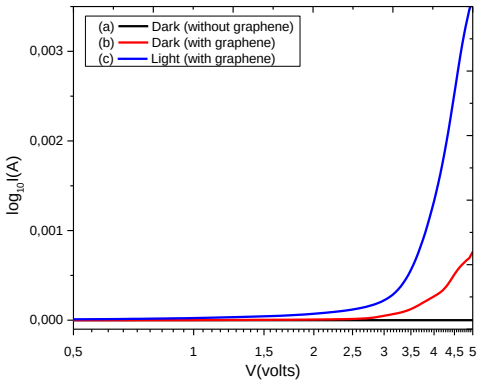

Fig. 7. IV graph of cubic SiC (a) dark (without graphene), (b) dark (with graphene), (c) light (with graphene).

4. Conclusion

3C-SiC is synthesized at relatively low temperature without using any catalyst, in a modified muffle furnace in the presence of argon. It is found that crystalline 3C-SiC is formed at 1480^{o}C. The average crystallite size of as-grown 3C-SiC is calculated by the sheerer method, sheerer plot method Williamson-Hall method, and Size Strain method are in accordance with each other. Raman, FTIR and UV-vis spectroscopy results confirmed the formation of 3C-SiC. I-V results of 3C-SiC with graphene contact has enhanced significantly the value of current (0.763mA) as compared to silver contacts. This further enhances the electrical conductivity to 3.57 mA when exposing to light. The present work suggested that the aforesaid method to grow 3C-SiC is a very simple technique for large scale production. Furthermore, IV measurements with illumination suggest that the grown sample (c) may enhance the photovoltaic properties through the formation of a schottky junction.

Acknowledgements

IRSIP (International research program Initiative program) HEC, Pakistanis highly for their financial support to first author. Thanks to N-Center, Sungkyunkwan University, South Korea for their major contribution in performing characterization.

References

[1] G. R. Yazdi, R. Vasiliauskas, T. Iakimov, A. Zakharov, M. Syväjärvi, R. Yakimova, Carbon N. Y. **57**, 477 (2013).
[2] F. Fuchs *et al.*, Sci. Rep. **3**(1), 1 (2013).
[3] J. Zhang, J. Chen, L. Xin, M. Wang, Mater. Sci. Eng. B Solid-State Mater. Adv. Technol. **179**(1), 6 (2014).
[4] T. Sri Devi Kumari, D. Jeyakumar, T. Prem Kumar, RSC Adv. **3**(35), 15028 (2013).
[5] L. Sun, C. Han, N. Wu, B. Wang, Y. Wang, RSC Adv. **8**(25), 13697 (2018).
[6] A. Guglya, A. Kalchenko, E. Lyubchenko, Y. Marchenko, A. Semenov, J. Nanotechnol., 1 (2018).
[7] M. Notarianni, J. Liu, K. Vernon, N. Motta, Beilstein Journal of Nanotechnology **7**(1), 149 (2016).
[8] L. K. S. Katsuhiko Ariga, Analyst, 2016.
[9] R. Yakimova, R. Vasiliauskas, J. Eriksson, M. Syväjärvi, Progress in 3C-SiC growth and novel

applications **711**, 3 (2012).
[10] P. K. Chu, J. yang Fan, Silicon Carbide Nanostructures, 2014.
[11] L. M. Shur, S. Rumyantsev, SIC Materials and Devices, 2006.
[12] S. C. Chiu, C. W. Huang, Y. Y. Li, J. Phys. Chem. C **111**(28), 10294 (2007).
[13] D. H. Duc, I. Naoki, F. Kazuyoshi, Int. J. Heat Mass Transf. **65**, 713 (2013).
[14] J. Li, Y. Zhang, Y. Kong, L. Hu, C. Jin, Z. Xi, Vacuum **146**, 87 (2017).
[15] H. Cheng, R. Tu, S. Zhang, M. Han, T. Goto, L. Zhang, J. Eur. Ceram. Soc. **37**(2), 509 (2017).
[16] H. Cheng et al., J. Eur. Ceram. Soc. **38**(9), 3057 (2018).
[17] S. B. Mishra, A. K. Mishra, R. W. Krause, B. B. Mamba, Mater. Lett. **63**(28), 2449 (2009).
[18] R. Sharma, D. V. S. Rao, V. D. Vankar, Mater. Lett. **62**(17-18), 3174 (2008).
[19] B. - W Lin, M. Imai, T. Yano, T. Iseki, J. Am. Ceram. Soc. **69**(4), C- 67 (1986).
[20] P. Kang et al., J. Alloys Compd. **604**, 304 (2014).
[21] S. Sugiyama, M. Togaya, J. Am. Ceram. Soc. **84**(12), 3013 (2001).
[22] M. Dragomir, M. Valant, M. Fanetti, Y. Mozharivskyj, RSC Adv. **6**(26), 21795 (2016).
[23] G. Mishra et al., J. Nanosci. Nanotechnol. **11**(6), 5049 (2011).
[24] J. Li, J. Tian, L. Dong, J. Eur. Ceram. Soc. **20**(11), 1853 (2000).
[25] B. Matovic et al., Mater. Lett. **164**, 68 (2016).
[26] B. Chayasombat, Y. Kimata, T. Tokunaga, K. Kuroda, K. Sasaki, Microsc. Microanal. **19**(5), 119 (2013).
[27] J. Wu, H. A. Becerril, Z. Bao, Z. Liu, Y. Chen, P. Peumans, Appl. Phys. Lett. **92**(26), 2008.
[28] Q. Ji et al., Angew. Chemie - Int. Ed. **49**(50), 9737 (2010).
[29] S. Watcharotone et al., NANO Lett. **7**(7), 1888 (2007).
[30] C. Gómez-Navarro et al., Nano Lett. **7**(11), 3499 (2007).
[31] M. Portail et al., J. Cryst. Growth **349**(1), 27 (2012).
[32] C. Atom, H. Atom, B. Gap, V. Kumar, Dangling Bond METAL ENCAPSULATED CLUSTERS, 2008.
[33] M. Zhang et al., J. Solid State Chem. **243**, 247 (2016).
[34] P. B. B. D. C. Hirsch, Phys. Bull. **8**(7), 237 (1957).
[35] N. Rani, S. Chahal, A. S. Chauhan, P. Kumar, R. Shukla, S. K. Singh, Mater. Today Proc. **12**, 543 (2019).
[36] M. A. Nawaz et al., Microstructural Study of As Grown And 650 O C Annealed Zno Nanorods: X-Ray Peak Profile Analysis **11**(2), 537 (2016).
[37] M. Kahouli, A. Barhoumi, A. Bouzid, A. Al-Hajry, S. Guermazi, Superlattices Microstruct. **85**, 7 (2015).
[38] J. W. Sun et al., Materials Science Forum **858**, 1028 (2016).
[39] P. Sharma, S. C. Katyal, Determination of optical parameters of a - (As 2 Se 3) 90 Ge 10 thin film, April, 2007.
[40] J. Jeong, K. Jang, H. S. Lee, G. S. Chung, G. yeol Kim, Phys. B Condens. Matter **404**(1), 7 (2009).
[41] J. M. Costantini, S. Miro, O. Pluchery, J. Phys. D. Appl. Phys. **50**(9), 2017.